Full paper

A current collector covering nanostructured villous oxygen-deficient NiO fabricated by rapid laser-scan for Li-O₂ batteries

Xiaowei Mu[a,1], Qiuhao Wen[b,1], Gang Ou[c], Yuemin Du[a], Ping He[a,*], Minlin Zhong[c], Hong Zhu[b], Hui Wu[c,*], Sixie Yang[a], Yijie Liu[a], Bojie Li[a], Xueping Zhang[a], Haoshen Zhou[a,d,**]

[a] Center of Energy Storage Materials & Technology, College of Engineering and Applied Sciences, National Laboratory of Solid State Microstructures, and Collaborative Innovation Center of Advanced Microstructures, Nanjing University, Nanjing 210093, PR China
[b] University of Michigan-Shanghai Jiao Tong University Joint Institute, Shanghai Jiao Tong University, Shanghai 200240, PR China
[c] State Key Laboratory of New Ceramics and Fine Processing, School of Materials Science and Engineering, Tsinghua University, Beijing 100084, PR China
[d] Energy Technology Research Institute, National Institute of Advanced Industrial Science and Technology (AIST), Umezono 1-1-1, Tsukuba 3058568, Japan

ARTICLE INFO

ABSTRACT

Non-aqueous Li-O₂ batteries attract extensive attention because of their ultra-high theoretical specific energy density. However, the high charge potential, which induces severe parasitic reactions such as the corrosion of carbon-based catalysts and metal current collectors, is one of the biggest challenges currently. Herein, a current collector of Ni foam covering nanostructured villous NiO with oxygen vacancies (NiO₁₋δ) was fabricated by a fast laser-scan technique. The modified NiO₁₋δ based current collector presented superior stability and comparable electrocatalytic activity. It delivered a discharge capacity of about $500\ \mathrm{mAh\ g^{-1}}$ and a low charge potential of $3.84\ \mathrm{V}$ in a Li-O₂ cell in the absence of catalysts. And this cell could maintain 73.5% of the initial capacity after 100 full discharge-charge cycles. Density functional theory (DFT) calculations verified that the improved electrocatalytic activity mainly derived from the introduction of oxygen vacancies in NiO₁₋δ. It improved the electronic conductivity for rapid electron transfer as well as served as active sites to bind O₂ and oxygen-containing intermediates (eg. LiO₂) for electrochemistry reactions. This work gives a rapid and easily mass-produced method to fabricate a stable and activated current collector for Li-O₂ batteries.

1. Introduction

Owing to their extremely high theoretical specific energy density ($\sim 3500\ \mathrm{Wh\ kg^{-1}}$), rechargeable non-aqueous lithium-oxygen (Li-O₂) batteries have captured worldwide attention [1–5]. They are promising to meet the power requirements of electric vehicles and smart grids, taking the place of traditional Li-ion batteries. Typically, in a Li-O₂ battery system, its operation depends on the reversible formation and decomposition of Li₂O₂ (Eq. (1)) [6–8]. However, lots of challenges must be addressed before their usage in practical applications. The primary challenge is the high charge potential in oxygen evolution reactions (OER) [9–13]. It has resulted in the low round-trip efficiency, detrimental degradation of electrolyte and poor cycle life. Therefore, multitudes of research efforts have been focused on combining effective catalysts and porous electrode structures to reduce the charging overpotential for non-aqueous Li-O₂ batteries [14–16].

$$2\mathrm{Li^+ + O_2 + 2e^- \leftrightarrow Li_2O_2}, \quad E^0 = 2.96V \tag{1}$$
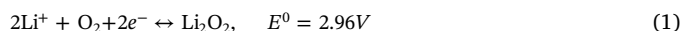
Based on previous reports, carbon based catalysts and carbon paper/cloth current collectors are widely applied in Li-O₂ batteries because of their high surface area, excellent electronic conductivity and superior oxygen reduction reaction (ORR) catalytic performance [17–19]. However, many studies demonstrated that carbon is susceptible to be corroded by the attack of reaction intermediated radicals and can actively promote the decomposition of electrolyte during cycling [17–20]. Hence, it is of necessity to elaborately design carbon-free cathodes, including carbon-free catalysts and current collectors, for Li-O₂ batteries to circumvent these parasitic reactions. Among varieties of carbon-free current collectors, Ni metal is most widely applied [21–24], which exhibits higher electronic conductivity over carbonaceous materials and metal oxides [25,26]. Nonetheless, different from carbon collectors, Ni metal shows little catalytic activity and makes no contribution to the battery performance. Besides, Ni metal is easily

oxidized inherently as a kind of active metals [27], especially when it is applied in an O_2-rich system with high oxidation potential. It has been reported that NiO possesses good activity towards the decomposition of both Li_2O_2 and Li_2CO_3 [21,28,29]. However, the electronic conductivity of NiO is inferior, which will undoubtedly increase the interface impedance and prevent the rapid charge transfer, leading to a high overpotential. Fortunately, in a recent literature, Ling et al. introduced oxygen vacancies into metal oxides, which is an effective way to significantly improve their electronic conductivity [30]. As a consequence, creating a covering layer of NiO with oxygen vacancies ($NiO_{1-\delta}$) on the Ni metal current collector is proposed to enhance its stability, electroconductivity and electrocatalytic activity in Li-O_2 batteries.

In the present work, we developed a one-pot fabrication of nanostructured villous $NiO_{1-\delta}$ layer grown on Ni foam collector directly by the fast laser-scan technique. The surface of Ni metal was protected effectively by the layer of $NiO_{1-\delta}$ nano-villi. Particularly, the electroconductivity and electrocatalytic activity of the whole Ni collector were promoted significantly. DFT calculations verified that the improved electrochemical performance mainly stemmed from the introduction of oxygen vacancies in NiO. It not only improved the electronic conductivity for rapid electron transfer [30], but also served as active sites to bind O_2 and oxygen-containing intermediates (eg. LiO_2) for electrochemistry reactions [31–35]. Moreover, a RF magnetron sputtering method was employed to deposit Ru nanoparticles onto the modified Ni collector to construct a self-standing carbon-free cathode. And superior discharge-charge performance with lower charge overpotential was obtained in Li-O_2 batteries.

2. Experimental section

2.1. Materials preparation

Ni foam was put on the substrate of the laser processing device (BX4II-E, Senged Laser). Then, it was irradiated by a linearly polarized ns laser with wavelength of 532 nm, repetition rate of 50 kHz, pulse duration of 12 ns and pulse energy of 0.4 mJ. A two mirror galvo scanner with an F-theta objective lens (f = 160 mm) was used to focus and scan the laser beam in the x-y directions. Here, $600\,\mathrm{mm\,s^{-1}}$ was adopted to tune the content of the oxide at the surface of Ni foam, which is the top irradiation speed we can carry out to keep the structural integrity. Besides, laser-scan speeds of 200 and $400\,\mathrm{mm\,s^{-1}}$ were also applied for comparison. After laser-scan treatments, the Ru nanoparticles were deposited on the surface of Ni foam by RF magnetron sputtering in 1 min with a constant power of 100 W. Pristine Ni foam functionalized with Ru nanoparticles without irradiation was also prepared. The process gas was pure argon at a pressure of 2.0 Pa, which was introduced into the chamber with a flow rate of 120 sccm. The Ni foam was positioned straight to the Ru target at a target-substrate distance of about 20 cm.

2.2. Characterization

Scanning electron microscopy (SEM) and transmission electron microscopy (TEM) images were taken on a Hitachi S-8010 (Tokyo, Japan) and JEOL JEM-2100 (Tokyo, Japan), respectively. The states of surface elements were characterized using X-ray photoelectron spectroscopy (XPS) spectra recorded by a Thermo Fisher Scientific Model K-Alpha spectrometer equipped with Al Ka radiation (1486.6 eV). Tauc plots were obtained based on the UV–Vis absorption spectra, which were acquired on a Shimadzu UV-3600 ultraviolet-visible spectrophotometer. The NiO contents were calculated based on the weight loss during the reduction of NiO into Ni under Ar/H_2 gas (H_2, 10 vol%) with a thermogravimetric analyzer (TG, Netzsch STA-449F3).

2.3. Electrochemical measurements

The Ni foam, LS-Ni foam, Ru@Ni foam and Ru@LS-Ni foam were used directly without any additional binder or conductive agent. CR2032-type coin cells with holes for oxygen-transfer were assembled in a glovebox filled with dry Ar to evaluate the electrochemical performance. And all the electrode material was dried at 80 °C overnight before assemblage. Tetraethyleneglycol dimethyl ether (TEGDME) (from Aldrich) mixed with $LiCF_3SO_3$ in a molar ratio of 4:1 was used as the electrolyte. LAND 2001A Battery Testing Systems (Wuhan LAND electronics Co., Ltd, P.R. China) were used for electrochemical performance tests. The capacities of the Li–O_2 batteries were normalized by the mass of NiO and the current densities applied were $100\,\mathrm{mA\,g^{-1}}$. Electrochemical impedance spectroscopy (EIS) Nyquist plots were measured with a frequency range of 100 kHz to 0.1 Hz and a scan rate of $10\,\mathrm{mV\,s^{-1}}$ by an electrochemical station (CHI440C, Shanghai Chenhua Co., Ltd, P.R. China). Mott-Schottky (M-S) tests were carried out by an electrochemical station (Zahner IM6) at a frequency of 1000 Hz in a typical three-electrode system with a saturated calomel reference electrode and a platinum plate counter electrode. And the electrolyte applied was the buffer solution of potassium phosphate (0.2 M, pH = 7).

2.4. Theoretical calculations

Spin-polarized DFT calculations were performed by using the Vienna ab initio simulation package (VASP) [36] with the projector augmented wave (PAW) method [37] and Perdew, Burke and Ernzerhof (PBE) functional [38]. The Hubbard-type U correction of Ni was taken into consideration and set to be 6.2 eV [39,40]. The most stable surface (100) of NiO was selected to be catalyst surface [41]. A six layers' slab with 2×1 lateral cells and a 10 Å vacuum along the z-direction was used to model the surface system. Cutoff energy was set 500 eV for the plane-wave basis set in all calculations. The Brillouin zone was sampled by $4 \times 8 \times 1$ Gamma centered mesh. Both layer thickness and k-point mesh here were tested to achieve a convergence of total energy within 0.01 eV. The top four layers of the slab were allowed to relax, the other two layers at bottom were fixed to mimic a bulk region. The convergence criteria for structural optimization was set to 0.1 eV/Å in force, while for the electronic step was set to 10^{-4} eV.

The adsorptions of O_2 and LiO_2 molecules on NiO surfaces as well as the electronic properties of slabs have been calculated. Herein adsorption energy ΔE is considered as the descriptor of binding strength. A negative value of ΔE suggests favorable adsorption, and it is determined by using Eq. (2),

$$\Delta E_M = E(NiO + M) - E(NiO) - E(M) \qquad (2)$$

where $E(NiO + M)$ and $E(NiO)$ represent the total energy of NiO system with and without the molecule M adsorbed on surface, respectively. Here M can be LiO_2 or O_2, and $E(M)$ represents the total energy of LiO_2, or gas phase O_2 molecule. Table S1 shows the calculation results of O_2 and LiO_2 adsorption.

3. Results and discussion

Herein, Ni foam was selected as the substrate material and treated by an elaborate method of laser-scan. Compared with other Ni metal collectors, Ni foam possesses 3D macroporous skeletons that favorably facilitate the rapid diffusion of O_2 and the effective infiltration of electrolyte for the whole energy conversion process. The laser treatment of Ni foam with size of 5 cm × 5 cm was completed within 7 min at the fast laser-scan speed ($600\,\mathrm{mm\,s^{-1}}$), clearly demonstrating the high preparation efficiency. And the color of Ni foam changed from silver white to deep black after laser-scan (Fig. 1a). Scanning electron microscopy (SEM) was utilized to characterize the architectures of Ni foam after laser-scan (denoted as LS-Ni foam) (Fig. 1b-d). It can be seen
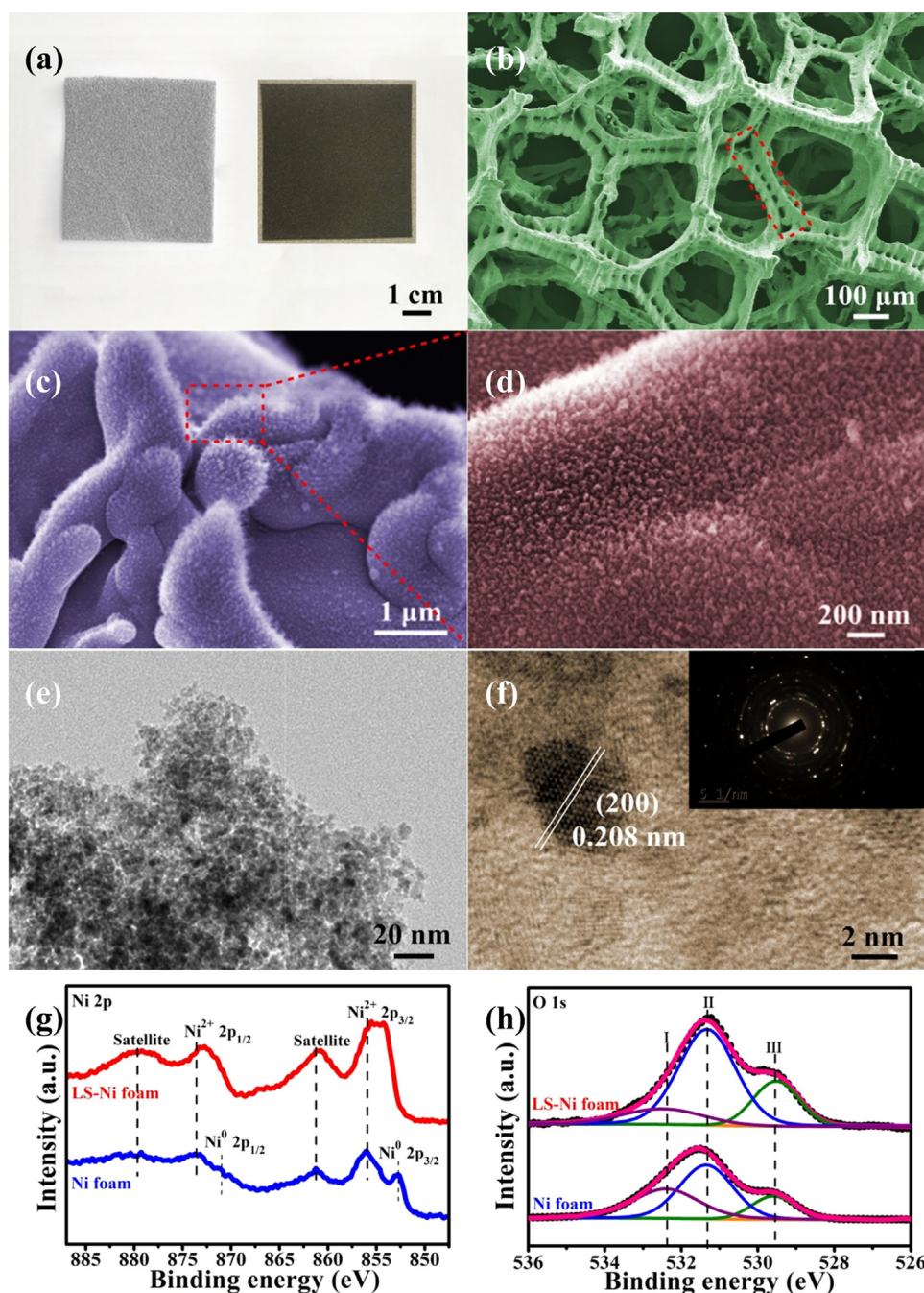
Fig. 1. (a) Digital photograph of Ni foams (5cm × 5cm) before (left) and after (right) laser-scan. (b-d) SEM images with low and high magnifications of the Ni foam after laser-scan. The red rectangle in (b) shows typical macropores on the Ni foam skeletons created by high energy laser beams. (e, f) TEM images with low and high magnifications of the Ni foam after laser-scan, corresponding SAED pattern is shown insert of (f). (g, h) XPS spectra of Ni foam before and after laser treatment, showing Ni 2p and O 1s spectrum, respectively.

that the LS-Ni foam has numerous macropores about 20 μm on the Ni foam skeletons, created by the high energy laser beam. Plenty of well-distributed nano-villi around 70 nm were produced on its surface, which efficiently increased the surface area and provided abundant active sites for electrochemical/chemical reactions. Transimission electron microscopy (TEM) was applied to further investigate the microstructures of LS-Ni foam. As shown in Fig. 1e, the villous layer was assembled by ultra-fine grains with diameter about 3 nm. According to the high-resolution transimission electron microscopy (HRTEM) image and its corresponding selected area electron diffraction (SAED) pattern (Fig. 1f), the crystal lattice spacing of the grains was estimated to be 0.208 nm, which is in accordance with the (200) facet of NiO. From the

XPS results, the Ni 2p spectrum of LS-Ni foam in Fig. 1g manifested satellite peaks of NiO, while the pristine Ni foam was partly oxidized with the coexistence of Ni^0. Note that the peaks of LS-Ni foam slightly shifted to right about 0.78 eV compared to that of Ni foam, which could arise from the introduction of oxygen vacancies [30,42]. Meanwhile, the O 1s spectra were divided into three peaks (Fig. 1h), denoted as I, II and III, which represent lattice oxygen, oxygen vacancies and absorbed oxygen pieces in NiO, respectively [43–45]. And the area of peak II in LS-Ni foam and pristine Ni foam accounted for 67.3% and 48.4% of the total constituents, respectively. The increased area ratio of peak II in LS-Ni foam indicated that a great deal of oxygen defects had been produced, in good consistence with Ni 2p spectra. Additionally, Ni foam
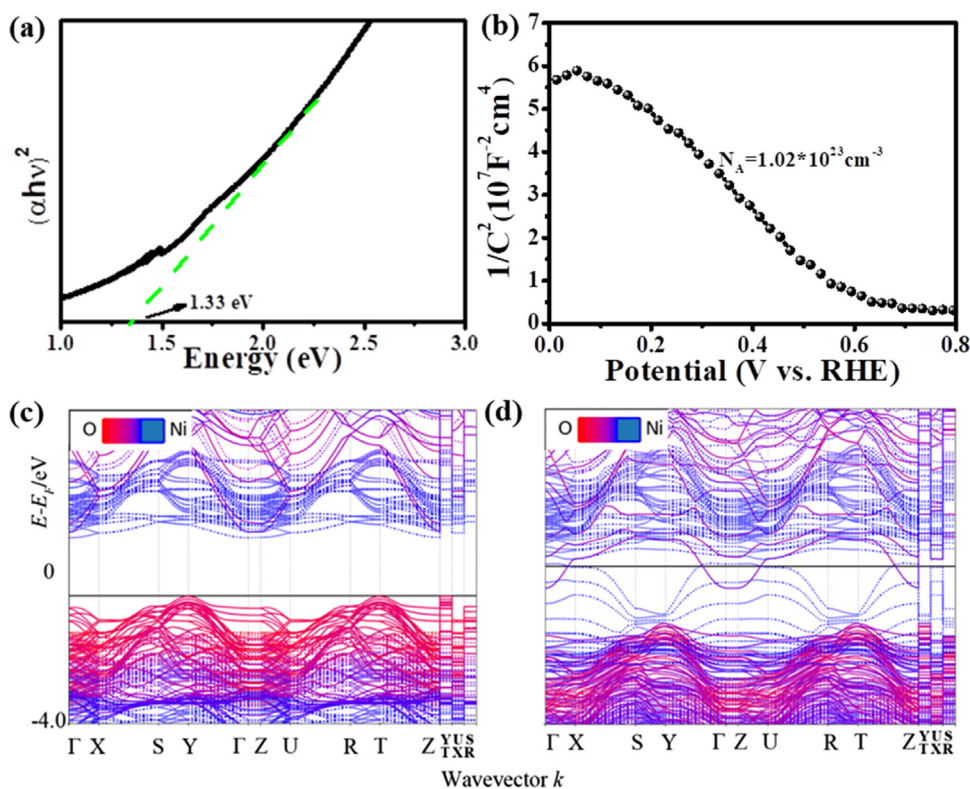
Fig. 2. (a) Tauc plot and (b) Mott-Schottky (M-S) plot of Ni foam after laser-scan. The fitted bandgap (1.33 eV) was much lower than that of the standard NiO (3.4 eV in principle). And the LS-Ni foam displayed typical p-type feature. The band structures of NiO (c) without oxygen vacancies and (d) with oxygen vacancies. After the introduction of oxygen vacancies, the bandgap decreased from 1.82 eV to 0.013 eV.
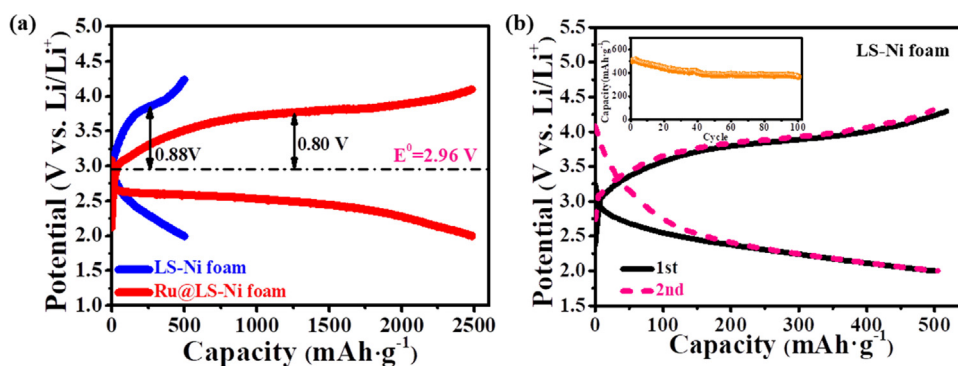
Fig. 3. (a) Galvanostatic discharge–charge profiles of Li-O$_2$ batteries with the LS-Ni foam collector and Ru@LS-Ni foam cathode. (b) Discharge–charge cyclic curves of the Li-O$_2$ battery with the LS-Ni foam collector, showing the first two circles. Inset is the variation of discharge capacity during the cycling.
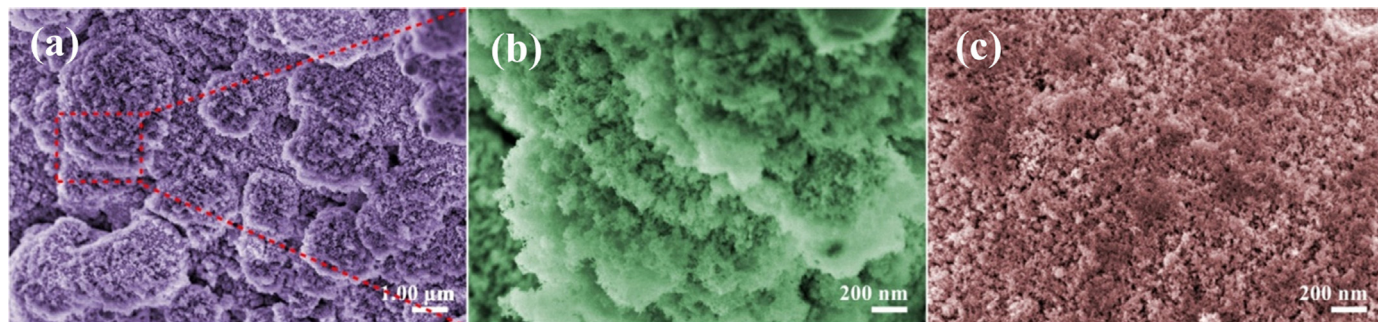
Fig. 4. SEM images the LS-Ni foam cathodes during different reaction stages. (a) low magnification and (b) high magnification after discharge, and (c) after recharge.

collectors with less oxygen vacancies (denoted as LS-Ni foam-2 and LS-Ni foam-4) were also fabricated by controlling the laser-scan speed of 200 and 400 mm s^{-1}. As shown in Fig. S1, the Ni peaks shifted to left about 0.27 eV and 0.15 eV compared to that in LS-Ni foam, and the area of peak II reduced to 56.3% and 58.0% in LS-Ni foam-2 and LS-Ni foam-

4, respectively.

It has been reported that the existence of oxygen vacancies can enhance the carrier concentration and thus improve the electronic conductivity of metal oxides, assuring a rapid charge-transfer and optimal adsorption energies for intermediates in ORR/OER [30]. From
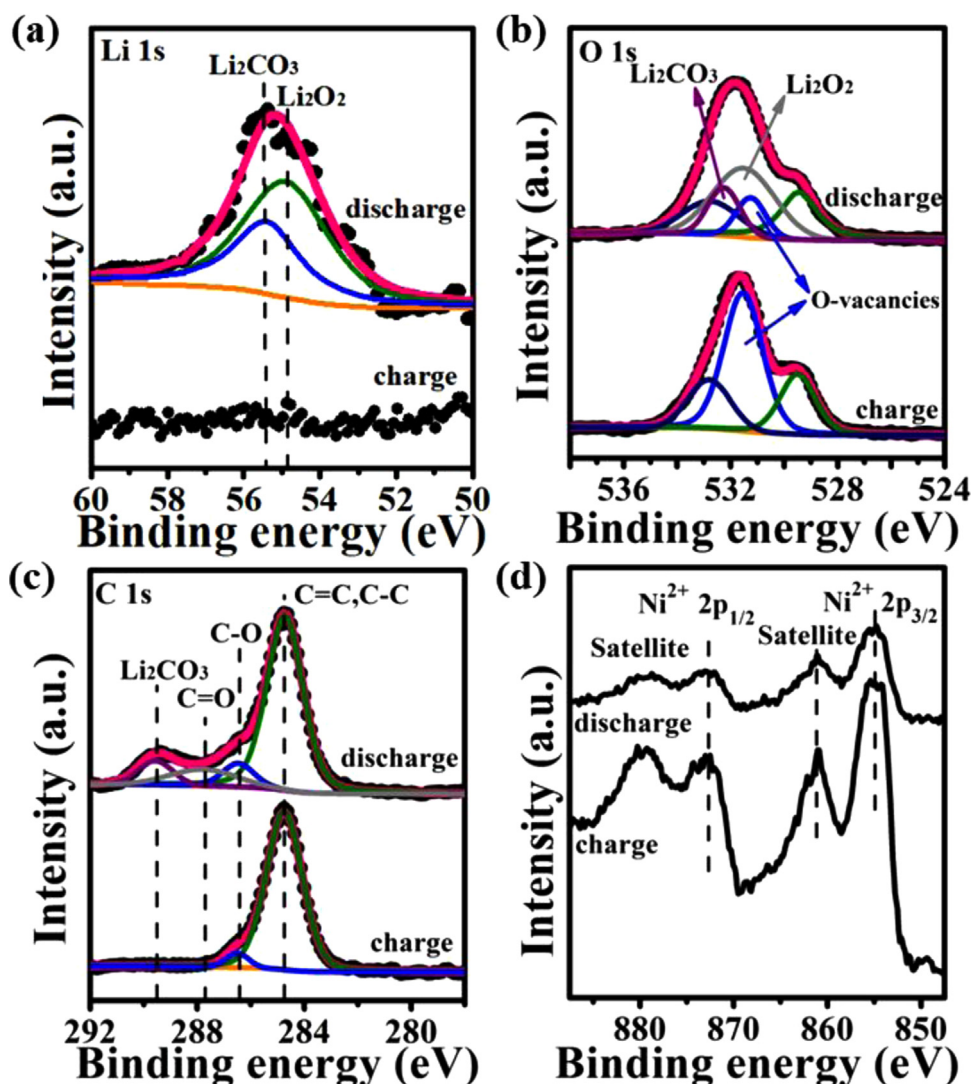
Fig. 5. XPS spectra of LS-Ni foam cathodes after discharge and charge, showing (a) Li 1s, (b) O 1s, (c) C 1s and (d) Ni 2p spectrum.

this point of view, Tauc plots and Mott-Schottky (M-S) plots were applied to measure the bandgap and carrier concentrations of prepared Ni foam collectors. From the Tauc plots (Fig. 2a and S2a), much narrowed bandgaps of 1.33 eV, 1.53 eV and 1.42 eV were obtained for LS-Ni foam, LS-Ni foam-2 and LS-Ni foam-4, respectively, in greatly contrast to that of standard NiO (3.4 eV of NiO in principle). These modified Ni foam collectors demonstrated tremendously promoted electronic conductivity after the introduction of oxygen vacancies. Besides, M-S plots all displayed typical p-type feature (Fig. 2b and S2b), suggesting that the charge carriers were predominant holes. According to Eq. (3),

$$\frac{dC^{-2}}{dV} = \frac{-2}{q\varepsilon_0\varepsilon_r N_A A^2}$$

(3)

where A is the surface area of the modified Ni foams and ε_r is the dielectric constant of NiO with the value of 11.9. The corresponding calculation results showed that holes concentrations of LS-Ni foam reached up to 1.02×10^{23} cm^{-3}, much more than those of LS-Ni foam-2 and LS-Ni foam-4 with the amount of 5.20×10^{20} cm^{-3} and 1.00×10^{21} cm^{-3}. And the higher carrier concentration of collectors is especially favorable for the charge-transfer process in electrochemical reactions.

Band structures of NiO with and without oxygen vacancies were calculated by DFT to further analyze the underlying mechanism of the promotion in electroconductivity. As for a perfect NiO slab shown in

Fig. 2c, the bandgap is relatively large about 1.82 eV and the fermi level is near the valence band maximum. These characteristics indicate that the conductivity of the NiO system is not good. The introduction of oxygen vacancies causes the defect states, shifts the Fermi level into the conduction band and hence increases the conductivity of the slab (Fig. 2d). Overall, the bandgap decreases after the introduction of oxygen vacancies, coinciding with the Tauc plot results. Moreover, electrochemical impedance spectroscopy (EIS) was applied to investigate the charge-transfer resistance of Ni foam and LS-Ni foam collectors in Li-O$_2$ batteries directly (Fig. S3). The corresponding equivalent circuit was shown in the inset image in Fig. S3, where R$_s$, CPE, R$_{ct}$ and W$_o$ represent the solution resistance, double-layer capacitance, charge-transfer resistance and Warburg impedance, respectively. According to the fitting results, the fitted R$_{ct}$ of Ni foam and LS-Ni foam were calculated to be 10856 and 155.3 Ω, respectively, which confirmed a better charge-transfer resistance after the introduction of oxygen vacancies.

It is widely acknowledged that most carbon current collectors exhibit certain electrocatalytic activity. With regard to the LS-Ni foam collectors, which possess properties including 3D porosity for mass-transfer, robust adhesion of NiO$_{1-\delta}$ from in-situ preparation, enhanced conductivity for charge-transfer and inherent electrochemical activity of NiO, the electrocatalytic performance of LS-Ni foam collectors in Li-O$_2$ batteries was evaluated. Full discharge-charge test with a cutoff
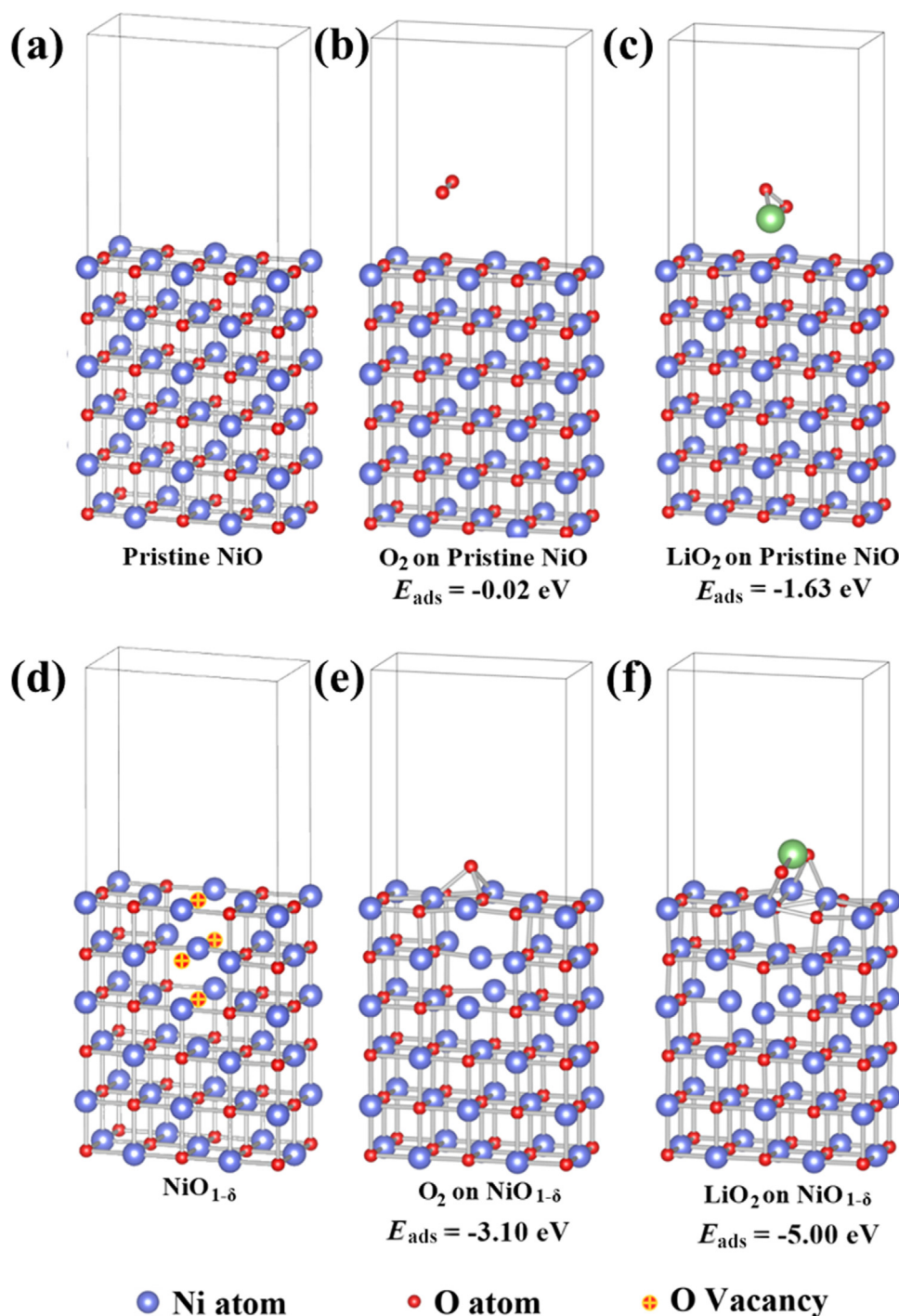
Fig. 6. The optimized structures of (a) NiO and (d) NiO$_{1-\delta}$ and corresponding binding energies of O$_2$ and LiO$_2$ on (b, c) NiO and (e, f) NiO$_{1-\delta}$. The binding energies of O$_2$ and LiO$_2$ on NiO$_{1-\delta}$ (-3.10 eV for O$_2$ and -5.00 eV for LiO$_2$) are much lower than those on perfect NiO (-0.02 eV for O$_2$ and -1.63 eV for LiO$_2$).

voltage of 2.0–4.3 V was performed (Fig. 3). The specific capacity was normalized by the mass of NiO, which was estimated based on the weight loss percent round 0.1% in TG curve (Fig. S4). And the current density adopted was 100 mA g^{-1}. The Li-O$_2$ battery with the LS-Ni foam collector delivered a discharge capacity approximately 500 mAh g^{-1}. And a relative low charge voltage plateau of 3.84 V was acquired. As shown in the inset of Fig. 3b, about 73.5% of the initial capacity was maintained even after 100 cycles. It suggested that the LS-NiO presented comparable electrochemical activity. While the galvanostatic discharge–charge profiles of the Li-O$_2$ batteries with the LS-Ni foam-2 and LS-Ni foam-4 current collectors are shown in Fig. S5. Initial

discharge capacity about 280 mAh g^{-1} and 400 mAh g^{-1} were delivered for LS-Ni foam-2 and LS-Ni foam-4, respectively, leading to 44% and 20% decrease in comparison with that of LS-Ni foam. Besides, both the charge and discharge overpotential were increased, revealing that the existence of more oxygen vacancies is favorable for ORR/OER electrochemistry.

Previously reports indicated that a lower charge voltage has less influence on parasitic reactions during charge, thus contributing to distinctly improved cycle stability [2,46]. The morphology and composition of LS-Ni foam collectors in Li-O$_2$ batteries during different reaction stages was studied by SEM and XPS. As shown in Fig. 4a, the
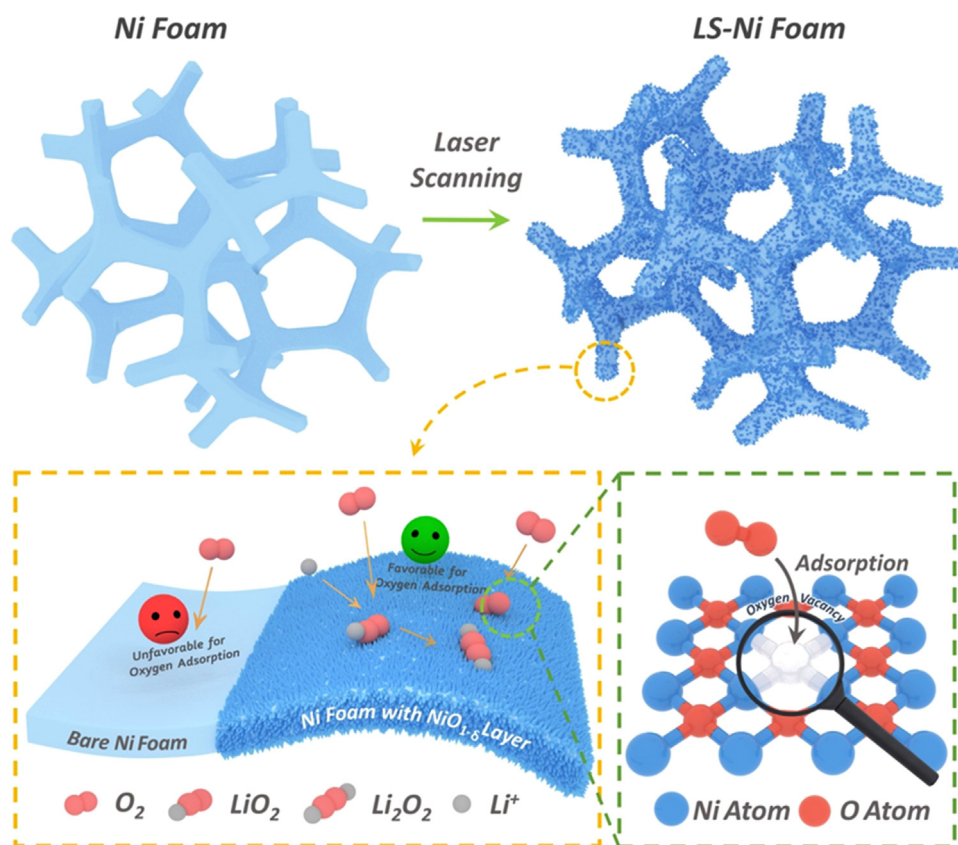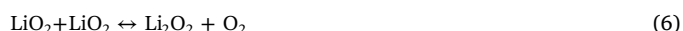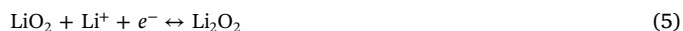
Fig. 7. Schematic illustration of the effect of oxygen vacancies in LS-Ni foam collector during the Li-O$_2$ battery operation.

discharge products exhibited rough conformal-like growth feature. From the enlarged image (Fig. 4b), the products were composed of porous and loose stacked flocculent structures, which facilitated most of the Li$_2$O$_2$ external surface to be exposed to the electrolyte directly and would be decomposed easier, thereby reducing the charge overpotential effectively. As recharge process finished (Fig. 4c), flocculent products disappeared completely and the cathode surface was recovered. XPS results demonstrated that the discharge products were mainly Li$_2$O$_2$ (Fig. 5a-c). Besides, some carbonate and carboxylate were produced by the decomposition of electrolyte, even though TEGDME is rather stable as reported [47]. Note that the peak intensity of oxygen vacancies reduced significantly after discharge compared with that of pristine LS-Ni foam, the ORR process probably preferred to occur on the vacancy places (discussed later). After recharge, the peaks of Li$_2$O$_2$ and Li$_2$CO$_3$ disappeared, revealing that NiO exhibited preferable effect on the decomposition of both Li$_2$O$_2$ and Li$_2$CO$_3$ [28]. Moreover, the peak positions in Ni 2p spectrum (Fig. 5d) showed no apparent change even after 100 cycles (Fig. S6), showing the electrochemical stability of NiO$_{1-\delta}$ during cycling.

DFT calculations were used to verify the elementary mechanism of Li-O$_2$ batteries and the roles of nano-villous NiO$_{1-\delta}$. Fig. 6 shows the optimized structures and corresponding binding energies of O$_2$ and LiO$_2$ on the surface of NiO and NiO$_{1-\delta}$, separately [48]. It was found that the binding energies of O$_2$ and LiO$_2$ on NiO$_{1-\delta}$ (-3.10 eV for O$_2$ and -5.00 eV for LiO$_2$) are much lower than those on perfect NiO (-0.02 eV for O$_2$ and -1.63 eV for LiO$_2$), indicating that reaction species are more easily captured by the surface of LS-Ni foam, thereby serving as active sites for the ORR/OER reactions [31–35]. Fig. 7 schematically illustrates the catalytic mechanism of nano-villous NiO$_{1-\delta}$ on LS-Ni foam during the Li-O$_2$ battery operation. Large amount of oxygen vacancies existing in the NiO$_{1-\delta}$ layer possess higher oxygen-bonding capability, serving as active sites to transfer electron and bind with O$_2$ and oxygen-containing intermediates (eg. LiO$_2$) for

electrochemistry reactions [31–35]. Hence, in the initial discharge stage, most O$_2$ binds to the surface of NiO$_{1-\delta}$ via oxygen vacancies, which is reduced through the one-electron process to form LiO$_2$ intermediate according to the Eq. (4). Few may exist in the electrolyte. LiO$_2$ is unstable and will get reduced and react with another Li$^+$ to form Li$_2$O$_2$ by the surface-adsorption path, following the Eq. (5). Those LiO$_2$ in electrolyte will disproportionate to Li$_2$O$_2$ by the chemistry process (Eq. (6)). Finally, flocculent discharge products in conformal-like growth form with loose and porous structures. Most of the Li$_2$O$_2$ external surface tend to be exposed to the electrolyte and thus to be decomposed easier in OER, accounting for a lower OER overpotential. In the subsequent charge process, Li$^+$ is extracted from Li$_2$O$_2$ to generate LiO$_2$, which binds with oxygen vacancies and gets rid of Li$^+$ and e$^-$ to release O$_2$ [35].

$$Li^+ + O_2 + e^- \leftrightarrow LiO_2 \tag{4}$$

$$LiO_2 + Li^+ + e^- \leftrightarrow Li_2O_2 \tag{5}$$

$$LiO_2 + LiO_2 \leftrightarrow Li_2O_2 + O_2 \tag{6}$$

Ru and Ru-based catalysts have been extensively reported to exhibit superior bifunctional catalytic activity for ORR/OER in Li-O$_2$ batteries [2,21,48,49]. However, the high mass density and cost restrict their widespread application. For the sake of cutting down the usage of Ru catalysts, herein a physical method of RF magnetron sputtering was employed. Trace amount of Ru nanoparticles with size around 30 nm were deposited on the LS-Ni foam collector to construct a self-standing carbon-free cathode (Fig. S7a). And XPS spectrum show that Ru existed in the form of elemental Ru and RuO$_x$ (Fig. S7b). The galvanostatic discharge–charge profile was shown in Fig. 3a. The Li-O$_2$ battery with the Ru@LS-Ni foam cathode delivered an increased discharge capacity of 2500 mAh g^{-1} and a reduced charge potential plateau about 3.76 V, suggesting the better electrocatalytic activity of Ru nanoparticles. For comparison, a Ru@Ni foam cathode using untreated Ni foam collector

was also fabricated. The Li-O$_2$ battery with the Ru@LS-Ni foam cathode exhibited discharge capacity ten times more than that of the Ru@Ni foam electrode (Fig. S8), demonstrating that the enhanced performance of Ru@LS-Ni foam came from the indispensable effect of NiO$_{1-\delta}$ layer besides the effect of Ru nanoparticles. And the Li-O$_2$ battery with the Ru@LS-Ni foam cathode showed excellent cycling stability as shown in Fig. S9. Even after 100 cycles, it still held a low charge plateau below 4.08 V. Furthermore, we also compared this work with the other Ni foam-based cathode materials from some published literatures, as shown in Table S2. Compared with those cathode materials, the Ru@LS-Ni foam cathode prepared in this work still shows the better electrochemical performance than the most of the Ni foam-based cathode materials reported in previous literatures.

4. Conclusions

In summary, nanostructured villous NiO with oxygen vacancies grown on the Ni foam was synthesized by adopting the fast, controllable and scalable laser-scan technique. Experiments and DFT calculations demonstrated that the introduction of oxygen vacancies not only improved the electronic conductivity for rapid electron transfer, but also served as active sites to bind O$_2$ and oxygen-containing intermediates (eg. LiO$_2$) for electrochemistry reactions. As a result, the Li-O$_2$ cell with the pristine LS-Ni foam collector delivered a discharge capacity of 500 mAh g^{-1} and a low charge potential about 3.84 V. And the cell could maintain 73.5% of the initial capacity after 100 full discharge-charge cycles. Then, the LS-Ni foam collector was functionalized with trace amount of Ru nanoparticles to construct a self-standing carbon-free cathode. The Li-O$_2$ battery using the Ru@LS-Ni foam cathode exhibited an increased discharge capacity up to 2500 mAh g^{-1} and a reduced charge potential about 3.76 V, which arrived from the catalytic activity of Ru nanoparticles and the indispensable effect of NiO$_{1-\delta}$ layer. In addition, this laser scanning technique can extended to fabricate a series of nanostructured metal oxides with oxygen vacancies by laser-scanning of corresponding metal substrates. It provides a new strategy for the fabrication of defective metal oxides with high catalytic activity in electrocatalysis and energy conversion and storage areas, such as metal-air batteries and water splitting.

Acknowledgements

Appendix A. Supporting information

Supplementary data associated with this article can be found in the online version at http://dx.doi.org/10.1016/j.nanoen.2018.06.043.

References

[1] P.G. Bruce, S.A. Freunberger, L.J. Hardwick, J.-M. Tarascon, Nat. Mater. 11 (2012) 19–29.
[2] Z.L. Jian, P. Liu, F.J. Li, P. He, X.W. Guo, M.W. Chen, H.S. Zhou, Angew. Chem. Int. Ed. 53 (2014) 442–446.
[3] A.C. Luntz, B.D. McCloskey, Chem. Rev. 114 (2014) 11721–11750.
[4] J. Lu, L. Li, J.B. Park, Y.K. Sun, F. Wu, K. Amine, Chem. Rev. 114 (2014) 5611–5640.
[5] D. Aurbach, B.D. McCloskey, L.F. Nazar, P.G. Bruce, Nat. Energy 1 (2016) 16128.
[6] K.M. Abraham, Z. Jiang, J. Electrochem. Soc. 143 (1996) 1–5.
[7] N.B. Aetukuri, B.D. McCloskey, J.M. García, L.E. Krupp, V. Viswanathan, A.C. Luntz, Nat. Chem. 7 (2015) 50–56.
[8] J. Lu, L. Cheng, K.C. Lau, E. Tyo, X. Luo, J. Wen, D. Miller, R.S. Assary, H.-H. Wang, P. Redfern, Nat. Commun. 5 (2014) 1.
[9] N.N. Feng, P. He, H.S. Zhou, Adv. Energy Mater. 6 (2016) 1502303.
[10] Y.C. Lu, B.M. Gallant, D.G. Kwabi, J.R. Harding, R.R. Mitchell, M.S. Whittingham, Y. Shao-Horn, Energy Environ. Sci. 6 (2013) 750–768.
[11] X.H. Yao, Q. Dong, Q.M. Cheng, D.W. Wang, Angew. Chem. Int. Ed. 55 (2016) 11344–11353.
[12] T. Liu, M. Leskes, W. Yu, A.J. Moore, L. Zhou, P.M. Bayley, G. Kim, C.P. Grey, Science 350 (2015) 530–533.
[13] Y. Li, X.G. Wang, S.M. Dong, X. Chen, G.L. Cui, Adv. Energy Mater. 6 (2016) 1600751.
[14] Y. Lu, H.X. Ang, Q.Y. Yan, E. Fong, Chem. Mater. 28 (2016) 5743–5752.
[15] S.M. Xu, Q.C. Zhu, M. Harris, T.H. Chen, C. Ma, X. Wei, H.S. Xu, Y.X. Zhou, Y.C. Cao, K.X. Wang, J.S. Chen, Nano Lett. 16 (2016) 5902–5908.
[16] B. Liu, P.F. Yan, W. Xu, J.M. Zheng, Y. He, L.L. Luo, M.E. Bowden, C.M. Wang, J.G. Zhang, Nano Lett. 16 (2016) 4932–4939.
[17] X.H. Yang, P. He, Y.Y. Xia, Electrochem. Commun. 11 (2009) 1127–1130.
[18] G. Wu, N.H. Mack, W. Gao, S. Ma, R. Zhong, J. Han, J.K. Baldwin, P. Zelenay, ACS Nano 6 (2012) 9764–9776.
[19] M.M.O. Thotiyl, S.A. Freunberger, Z.Q. Peng, P.G. Bruce, J. Am. Chem. Soc. 135 (2012) 494–500.
[20] R.A. Wong, A. Dutta, C.Z. Yang, K. Yamanaka, T. Ohta, A. Nakao, K. Waki, H.R. Byon, Chem. Mater. 28 (2016) 8006–8015.
[21] P. Tan, Z.H. Wei, W. Shyy, T.S. Zhao, X.B. Zhu, Energy Environ. Sci. 9 (2016) 1783–1793.
[22] X.Y. Yang, J.J. Xu, Z.W. Chang, D. Bao, Y.B. Yin, T. Liu, J.M. Yan, D.P. Liu, Y. Zhang, X.B. Zhang, Adv. Energy Mater. (2018).
[23] W.B. Luo, X.W. Gao, D.Q. Shi, S.L. Chou, J.Z. Wang, H.K. Liu, Small 12 (2016) 3031–3038.
[24] Q.C. Zhu, S.M. Xu, M.M. Harris, C. Ma, Y.S. Liu, X. Wei, H.S. Xu, Y.X. Zhou, Adv. Funct. Mater. 26 (2016) 8514–8520.
[25] Å. Andersson, O. Hunderi, C.G. Granqvist, J. Appl. Phys. 51 (1980) 754–764.
[26] Q.L. Hu, Y.J. Choi, C.J. Kang, H.L. Lee, T.-S. Yoon, J. Ind. Eng. Chem. 24 (2015) 293–296.
[27] X.C. Fu, W.X. Shen, T.Y. Yao, Phys. Chem. Beijing (1990).
[28] S.F. Tong, M.B. Zheng, Y. Lu, Z.X. Lin, J. Li, X.P. Zhang, Y. Shi, P. He, H.S. Zhou, J. Mater. Chem. A 3 (2015) 16177–16182.
[29] M. Hong, H.C. Choi, H.R. Byon, Chem. Mater. 27 (2015) 2234–2241.
[30] T. Ling, D.Y. Yanl, Y. Jiao, H. Wang, Y. Zheng, X.L. Zheng, J. Mao, X.W. Du, Z.P. Hu, M. Jaroniec, S.Z. Qiao, Nat. Commun. 7 (2016) 12876.
[31] H. Yadegari, M.N. Banis, A. Lushington, Q. Sun, R.Y. Li, T.K. Sham, X.L. Sun, Energy Environ. Sci. 10 (2017) 286–295.
[32] S.H. Oh, R. Black, E. Pomerantseva, J.H. Lee, L.F. Nazar, Nat. Chem. 4 (2012) 1004–1010.
[33] R. Gao, L. Liu, Z.B. Hu, P. Zhang, X.Z. Cao, B.Y. Wang, X.F. Liu, J. Mater. Chem. A 3 (2015) 17598–17605.
[34] F. Wang, H.J. Li, Q.X. Wu, J. Fang, Y. Huang, C.L. Yin, Y.H. Xu, Z.K. Luo, Electrochim. Acta 202 (2016) 1.
[35] J.B. Zhang, C.F. Zhang, W. Li, Q. Guo, H.C. Gao, Y. You, Y.T. Li, Z.M. Cui, K.-C. Jiang, H.J. Lo ng, D.W. Zhang, S. Xin, ACS Appl. Mater. Interfaces (2018).
[36] J. Furthmüller, G. Kresse, Phys. Rev. B 54 (1996) 11169–11186.
[37] P.E. Blöchl, Phys. Rev. B 50 (1994) 17953–17979.
[38] K. Burke, M. Ernzerhof, J.P. Perdew, Phys. Rev. Lett. 77 (1996) 3865–3868.
[39] V.I. Anisimov, J. Zaanen, O.K. Andersen, Phys. Rev. B Condens. Matter 44 (1991) 943.
[40] Y. Gao, X. Wang, J. Ma, Z. Wang, L. Chen, Chem. Mater. 27 (2015) 3456–3461.
[41] D. Su, M. Ford, G. Wang, Sci. Rep. 2 (2012) 924.
[42] R. Gao, Z.Y. Li, X.L. Zhang, J.C. Zhang, Z.B. Hu, X.F. Liu, ACS Catal. 6 (2016) 400–406.
[43] G. Ou, P.X. Fan, H.J. Zhang, K. Huang, C. Yang, W. Yu, H.H. Wei, M.L. Zhong, H. Wu, Y.D. Li, Nano Energy 35 (2017) 207–214.
[44] S. Kim, J. Lee, H. Ahn, H. Song, J. Jang, ACS Appl. Mater. Interfaces 5 (2013) 1596–1603.
[45] B.P. Payne, M.C. Biesinger, N.S. McIntyre, J. Electron Spectrosc. 175 (2009) 55–65.
[46] J.J. Xu, Z.L. Wang, D. Xu, L.L. Zhang, X.B. Zhang, Nat. Commun. 4 (2013) 2438.
[47] B.D. Adams, R. Black, Z. Williams, R. Fernandes, M. Cuisinier, E.J. Berg, P. Novak, G.K. Murphy, L.F. Nazar, Adv. Energy Mater. 5 (2015) 1400867.
[48] J.J. Xu, Z.W. Chang, Y. Wang, D.P. Liu, Y. Zhang, X.B. Zhang, Adv. Mater. 28 (2016) 9620–9628.
[49] J. Jiang, P. He, S.F. Tong, M.B. Zheng, Z.X. Lin, X.P. Zhang, Y. Shi, H.S. Zhou, NPG Asia Mater. 8 (2016) e239.